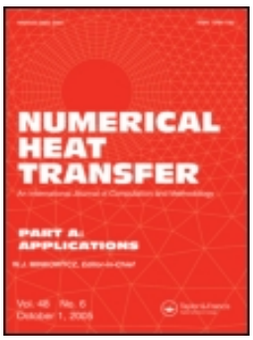

Taylor & Francis
Taylor & Francis Group

Numerical Heat Transfer, Part A: Applications
An International Journal of Computation and Methodology

ISSN: 1040-7782 (Print) 1521-0634 (Online) Journal homepage: http://www.tandfonline.com/loi/unht20

Numerical Simulation of Bubble Dynamics in a Uniform Electric Field by the Adaptive 3D-VOSET Method

Tai Wang , Huixiong Li , Yifan Zhang & Dongxiao Shi

To cite this article: Tai Wang , Huixiong Li , Yifan Zhang & Dongxiao Shi (2015) Numerical Simulation of Bubble Dynamics in a Uniform Electric Field by the Adaptive 3D-VOSET Method, Numerical Heat Transfer, Part A: Applications, 67:12, 1352-1369, DOI: 10.1080/10407782.2014.965116

To link to this article: https://doi.org/10.1080/10407782.2014.965116

Numerical Heat Transfer, Part A, 67: 1352–1369, 2015

ISSN: 1040-7782 print/1521-0634 online
DOI: 10.1080/10407782.2014.965116

Taylor & Francis
Taylor & Francis Group

NUMERICAL SIMULATION OF BUBBLE DYNAMICS IN A UNIFORM ELECTRIC FIELD BY THE ADAPTIVE 3D-VOSET METHOD

Tai Wang, Huixiong Li, Yifan Zhang, and Dongxiao Shi
State Key Laboratory of Multiphase Flow in Power Engineering, Xi'an Jiaotong University, Xi'an, Shaanxi, P. R. China

This article presents a three-dimensional numerical simulation of the effect of a uniform electric field on the dynamics of bubbles in a viscous fluid. The two-phase interface is captured utilizing a coupled volume-of-fluid and level set (VOSET) method by solving the full Navier–Stokes equations coupled with electric field equations. To track the interface more accurately, the dynamically adaptive octree grids are used to refine the grids around the interface. The effects of different parameters such as the electric Bond number, the ratio of electrical permittivity, the gravitational Bond number, and the Reynolds number on the motion and deformation of the bubble are investigated. According to the computational results, it is found that the electric field has a significant influence on the bubble dynamic behavior. Increase of the electric Bond number or the ratio of electrical permittivity results in the larger deformation and rising velocity of the bubble. For a higher electric Bond number and the Reynolds number, separations of the tail of the bubble are observed. In this case, the jet above the bubble is strong enough to turn the spherical bubble to a toroidal shape.

1. INTRODUCTION

Gas–liquid two-phase flows are frequently encountered in many engineering applications such as energy and power engineering, chemical engineering, nuclear reactor, and space engineering. The motion, deformation, break-up, and coalescence of bubbles, which are elementary phenomena in gas–liquid two-phase flows, play an important role in the heat and mass transfer, chemical reaction, and other applications of the two-phase media. In the past few years, dynamics of the bubble in a viscosity fluid has been experimentally investigated by numerous researchers [1–3]. For example, Clift et al. [1] studied the factors determining the shape and rising velocity of the bubbles. Wu and Gharib [2] reported the experimental results of the shape and path of a small bubble rising in clean water. Brereton and Korotney [3] presented the experimental results of the coaxial coalescence and oblique coalescence of two gas bubbles in an initially quiescent liquid and analyzed the difference between the

Received 24 June 2014; accepted 26 July 2014.

Address correspondence to Huixiong Li, State Key Laboratory of Multiphase Flow in Power Engineering, Xi'an Jiaotong University, No. 28 Xianning West Road, Xi'an, Shaanxi, 710049 P. R. China. E-mail: huixiong@mail.xjtu.edu.cn

Color versions of one or more of the figures in the article can be found online at www.tandfonline.com/unht.

NOMENCLATURE

A_W	largest horizontal cross-section of the bubble, m^2	W	bubble width, m
Bo	gravitational Bond number	x, y, z	coordinates
Bo_e	electric Bond number	$\delta(\phi)$	delta function
C	volume fraction	Δ	grid size, m
$\mathbf{E}$	electric field intensity, N/C	μ	viscosity, Pa·s
$\mathbf{F}_e$	electric force, N/m^3	κ	curvature
$\mathbf{F}_\sigma$	surface tension force, N/m^3	ε	relative permittivity of material
$\mathbf{g}$	gravitational acceleration, m/s^2	ε_0	permittivity of vacuum, F/m
$H(\phi)$	Heaviside function	ρ	density, kg/m^3
H	bubble height, m	σ	surface tension coefficient, N/m
$\mathbf{n}$	unit normal vector	ϕ	level set function
p	pressure, Pa	ψ	electric potential
R	radius, m	λ_ρ	ratio of density
Re	Reynolds number	λ_μ	ratio of viscosity
t	time, s	λ_ε	ratio of permittivity
T	dimensionless time	**Subscripts**	
$\mathbf{u}$	velocity vector, m/s	c	continuous phase
		d	dispersed phase

shapes of the leading bubble and that of the following bubble. Besides the amounts of experimental investigations, numerical simulations of the bubble dynamics have been performed. Luz et al. [4] numerically studied the deformation and velocity of a bubble. Van Sint Annaland et al. [5] simulated the coaxial coalescence and oblique coalescence of two gas bubbles and compared with the experimental results of the literature [3]. Although much work has been done to investigate bubble dynamics, the bubble motion under external force including electric force or magnetic force has not been sufficiently studied.

Imposing an external electric field is a good method for manipulating the motion, deformation, and velocity of bubbles, which can enhance nucleate boiling heat transfer. Many experimental methods [6–11] and numerical methods [12–15] are applied to investigate the growth and departure of bubbles under electric fields. Sarnobat et al. [6] presented the experimental results of the growth of nitrogen bubbles from a single nozzle in glycerol. Iacona et al. [8] studied the effect of electric fields on the detachment of bubbles under microgravity. The results show that the increase of the electric fields leads to the decrease of the bubble volume at detachment. Gao et al. [11] reported the experimental investigations of the R113 bubble nucleation and growth dynamic under nonuniform electric field. Zhang et al. [14] used a volume-of-fluid (VOF) method and a nonorthogonal body-fitted mesh system to study the effect of electric field on the heat transfer and bubble deformation in nucleate boiling. Sunder et al. [15] performed a direct numerical simulation of the growth and coalescence of bubbles under a nonuniform electric field and found that appropriate electrode configurations can reduce the bubble volume at detachment. The growth and detachment of bubbles under electric fields have been extensively studied, but the literature [16, 17] about the motion and deformation of the rising bubbles is limited. Mahlmann and Papageorgiou [16] used a two-dimensional (2D) level set (LS) method to simulate a bubble rising in a quiescent liquid. Yang et al.

[17] studied the effect of the direction of electric fields on the motion and deformation of the bubble.

Owing to the restriction of the experimental conditions and the improvement of computer performance, the numerical methods have become increasingly popular in the investigations of two-phase flow. The boundary integral method [18–20], front tracking method [21–24], VOF method [14, 25, 26], LS method [16, 27–29], and phase field method [17, 30, 31] have been extended to simulate the two-phase flow under the electric field. Boundary integral method and front tracking method are explicit methods that can accurately calculate body force, but implementing these methods is very complicated. The VOF method, LS method, and phase field method are implicit methods that can routinely handle the topological changes of interface such as break-up and coalescence. In contrast to the phase field method, the VOF and LS methods have been widely used in electrohydrodynamics. The LS method can accurately calculate the interface normal and curvature and this method can also smooth the physical properties around the interfaces, but it cannot conserve mass. However, the VOF method can conserve mass, but it cannot accurately calculate the parameters around the interface. To overcome these disadvantages, the Coupled Level Set and Volume of Fluid (CLSVOF) [32–36] method, which combines the VOF method and the LS method, was developed and has been successfully implemented in electrohydrodynamics. Another coupled VOF and levels set (VOSET) method [37–39], in which only the VOF advection equation is solved, also was proposed and has been used to simulate droplet dynamics under magnetic field.

In this article, we adopt a 3D-VOSET method to simulate the motion, deformation, rising, and break-up of an initially spherical bubble in a quiescent viscous fluid under a uniform electric field. To improve the accuracy of the calculation and save the computer resources, the adaptive octree grid method [40–42] is used to refine the grids around the interface. If the interface changes, the grid system will be adjusted to meet the adaptive criterion that the interface must lay on the densest grid. The Poisson equation for the electric field is solved to calculate the electric force. The surface tension force and electric force are added to the Navier–Stokes (N–S) equations, which are solved by the finite-volume method. To verify the program code, the equilibrium shape of a droplet in uniform electric fields is numerically simulated and compared with the results calculated by a minimum energy approach [43]. Then, we investigate the effects of the electric field, ratio of electrical permittivity, surface tension coefficient, and viscosity on the bubble motion and deformation.

2. MATHEMATICAL FORMULATIONS AND PHYSICAL MODELS

2.1. Governing Equations

For fluid flows under electric fields, the fluid flows are governed by inertial force, viscous force, electric force, and so on. With the assumption of immiscible, incompressible Newtonian fluids, the N–S equation is expressed as

$$\nabla \cdot \mathbf{u} = 0 \tag{1}$$

$$\rho\left(\frac{\partial \mathbf{u}}{\partial t} + \mathbf{u} \cdot \nabla \mathbf{u}\right) = -\nabla p + \rho \mathbf{g} + \nabla \cdot \left[\mu\left(\nabla \mathbf{u} + (\nabla \mathbf{u})^{\mathbf{T}}\right)\right] + \mathbf{F}_{\sigma} + \mathbf{F}_{\mathrm{e}} \tag{2}$$

where ρ is the fluid density, $\mathbf{u}$ is the velocity vector, μ is the fluid viscosity, p is the pressure, and $\mathbf{g}$ is the gravitational acceleration. $\mathbf{F}_\sigma$ and $\mathbf{F}_e$ are the surface tension force and the electric force, respectively.

2.2. The 3D-VOSET Method

The VOSET method, which is a coupled VOF and LS methods, is developed by Sun et al. [37]. In this method, only the VOF advection equation needs to be solved, while the LS function is calculated by a simple iterative geometric operation. Recently, Wang et al. [38] have successfully implemented the 2D-VOSET method on adaptive quadtree grid system. Here, we have developed a 3D-VOSET method on an adaptive octree grid system and used it to simulate dynamics of the bubble in electric fields.

The interface is identified by a volume fraction C defined as the ratio of the dispersed volume and the total volume of a cell. If the cell is filled with dispersed phase, the value of C is 1. If the cell is filled with continuous phase, the value of C is 0. If the cell contains the interface, the value of C varies between 0 and 1. The transport equation of the volume fraction C is written as

$$\frac{\partial C}{\partial t} + \mathbf{u} \cdot \nabla C = 0 \tag{3}$$

In this article, the interface is reconstructed by the 3D-PLIC method described in more detail by Wang et al. [44]. After reconstructing the interface shapes and positions, the LS function ϕ is calculated by a simple geometric method [36]. The LS function ϕ is only calculated in the region of four times width of the grid on each side of the interface. The calculation of the LS function ϕ is an iterative procedure, and the details of the VOSET method are available in the literature [37, 38].

The density ρ and viscosity η can be calculated by a weighted arithmetic mean interpolation.

$$\rho = \rho_c H(\phi) + \rho_d (1 - H(\phi)) \tag{4}$$

$$\mu = \mu_c H(\phi) + \mu_d (1 - H(\phi)) \tag{5}$$

and the relative permittivity (ε) of the material is calculated by a weighted harmonic mean interpolation.

$$\frac{1}{\varepsilon} = \frac{H(\phi)}{\varepsilon_c} + \frac{1 - H(\phi)}{\varepsilon_d} \tag{6}$$

where the subscripts c and d refer to the continuous and dispersed phases, respectively. $H(\phi)$ is the Heaviside function, which is given by

$$H(\phi) = \begin{cases} 0 & \text{if } \phi < -\gamma \\ \frac{1}{2}\left[1 + \frac{\phi}{\gamma} + \frac{1}{\pi}\sin\left(\frac{\pi\phi}{\gamma}\right)\right] & \text{if } |\phi| \le \gamma \\ 1 & \text{if } \phi > \gamma \end{cases} \tag{7}$$

where γ is a tuneable parameter to determine the size of the bandwidth for numerical smearing. In this article, γ equals to 1.5Δ and Δ is the grid size.

In addition, the surface tension force in Eq. (2) is calculated by the continuum surface force (CSF) model [45].

$$\mathbf{F}_\sigma = -\sigma\kappa(\phi)\delta(\phi)\nabla\phi \tag{8}$$

where σ is the surface tension coefficient and ϕ is the LS function. The interface curvature κ is calculated from

$$\kappa = \nabla \cdot (\mathbf{n}), \mathbf{n} = \frac{\nabla\phi}{|\nabla\phi|} \tag{9}$$

where $\mathbf{n}$ is the interface normal vector.

The Dirac distribution function $\delta(\phi)$ is defined as

$$\delta(\phi) = \begin{cases} 0 & \text{if} |\phi| > \gamma \\ \frac{1}{2\gamma}\left[1 + \cos\left(\frac{\pi\phi}{\gamma}\right)\right] & \text{if} |\phi| \leq \gamma \end{cases} \tag{10}$$

2.3. The Electric Field Model

In electrohydrodynamics, the electric field intensity $\mathbf{E}$ is assumed to be irrotational ($\nabla \times \mathbf{E} = 0$) because the effect of magnetic induction is negligible. For a perfect dielectric material, the electric field intensity $\mathbf{E}$ can be solved by

$$\nabla \cdot (\varepsilon\varepsilon_0\mathbf{E}) = 0 \tag{11}$$

where ε_0 is the permittivity of the vacuum and ε is the relative permittivity of the material. The electric field intensity $\mathbf{E}$ can be defined as a gradient in the potential field (ψ), $\mathbf{E} = -\nabla\psi$. Equation (11) can be rewritten as

$$\nabla \cdot (\varepsilon\varepsilon_0\nabla\psi) = 0 \tag{12}$$

The electric force $\mathbf{F}_e$ in Eq. (2) can be calculated by the following equation.

$$\mathbf{F}_e = -\frac{1}{2}\varepsilon_0\mathbf{E}^2\nabla\varepsilon \tag{13}$$

2.4. Numerical Details

The 3D model applied to investigate the bubble dynamic is shown in Figure 1. A bubble with an initial radius $R = 0.004$ is located at a rectangular computational domain of ($8R \times 8R \times 16R$) and is released from the position ($4R$, $4R$, $4R$). A uniform electric field is imposed in the z-direction. The electric potential is ψ_0 on the top boundary and 0 at the bottom boundary. Other boundaries of the computational

domain are Neumann boundary conditions, and no-slip boundary conditions are applied at all walls.

The rising of bubbles in a uniform electric field can be characterized by the dimensionless parameters, including Reynolds (Re) number, gravitational Bond (Bo) number, electric Bond (Bo_e) number, and the ratios of properties of the continuous phase and the dispersed phase, which are given by

$$Re = \frac{\rho_c\sqrt{R^3\mathbf{g}}}{\mu_c}, Bo = \frac{\rho_c\mathbf{g}R^2}{\sigma}, Bo_e = \frac{\varepsilon_0\varepsilon_c\mathbf{E}_0^2R}{\sigma}, \lambda_\rho = \frac{\rho_c}{\rho_d}, \lambda_\mu = \frac{\mu_c}{\mu_d}, \lambda_\varepsilon = \frac{\varepsilon_c}{\varepsilon_d} \tag{14}$$

To investigate the grid dependency of the results, different grid systems are used to simulate a rising bubble under the conditions of $Re = 2$, $Bo = 2$, $Bo_e = 15$, $\lambda_\rho = 100$, $\lambda_\mu = 100$, and $\lambda_\varepsilon = 3$. The results of the grid-independent tests are listed in Table 1. The base grid (first level) in case D is $20 \times 20 \times 40$, where four grid levels are applied, the grid resolution is $R/\Delta = 20$, and the number of the cells at the initial time (N_{ig}) is 145,696. However, to keep the same resolution, the number of the cells for the uniform grid system (N_{ug}) should be 8,192,000. The grid information of case A$\sim$C can also be found in Table 1. The numerical simulations are performed on a Core i7 with 3.4 GHz until dimensionless time ($T = t/\sqrt{R/\mathbf{g}}$) of $T = 8$, also the computational costs (CPU time) are obtained. Figure 2 compares the shapes of the bubble for case A$\sim$D; it can be seen that the difference in the bubble shape gradually decreases with the increase of R/Δ and has no significant change when the grid resolution $R/\Delta \geq 15$. Considering the accuracy of calculation and the cost of computer resources, the grid resolution $R/\Delta = 15$ is adopted in this article.

To further verify the program code, the equilibrium shape of a droplet in uniform electric fields is numerically simulated and compared with the results calculated by a minimum energy approach [43]. A stationary spherical droplet with radius R is positioned at the center of a domain of $10R \times 10R \times 10R$. The surrounding fluid and the droplet have the same density and viscosity, and the ratio of permittivity λ_ε equals 0.2. Different uniform electric fields are imposed in the vertical direction, and the gravity is not considered. The comparison between the numerical and the theoretical results of the droplet shapes under different Bo_e is shown in Figure 3. The numerical results are in good agreement with the theoretical results; thus, it is concluded that the developed numerical model in this article can be further used to study the two-phase flows under uniform electric fields.

Table 1. Results of the grid-independent tests

Case	Base grid	Level	R/Δ	N_{ig}	N_{ug}	CPU time/h
A	$20 \times 20 \times 40$	2	5	27,032	128,000	5
B	$20 \times 20 \times 40$	3	10	52,232	1,024,000	19
C	$30 \times 30 \times 60$	3	15	127,640	3,456,000	62
D	$20 \times 20 \times 40$	4	20	145,696	8,192,000	109

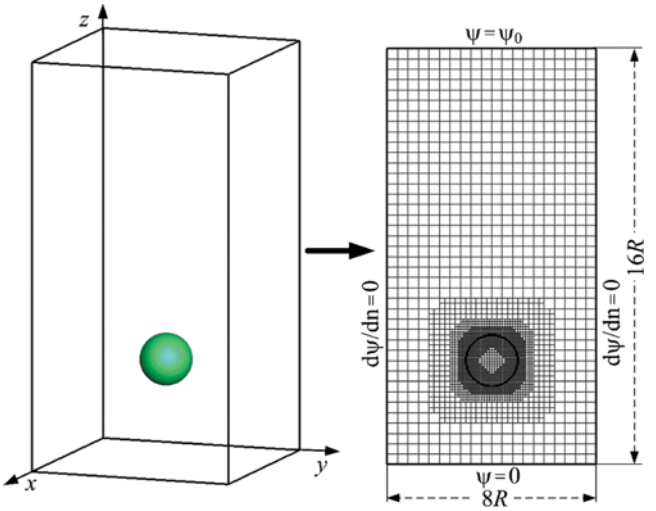

Figure 1. Schematic of the 3D model of the rising of a bubble in a uniform electric field.

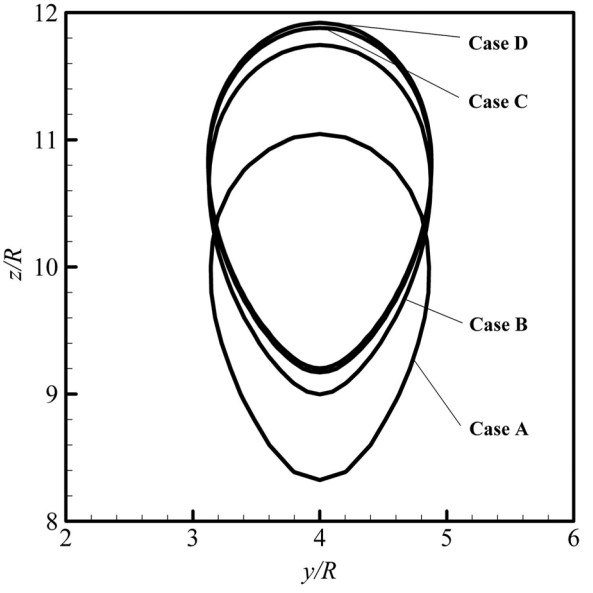

Figure 2. Bubble shapes with different grid sizes at $T = 8$.

3. RESULTS AND DISCUSSION

In this section, we present the numerical results of the deformation and rising of an initially spherical bubble in a quiescent viscous fluid under a uniform electric field. In electrohydrodynamics, the motion and deformation of the bubble under

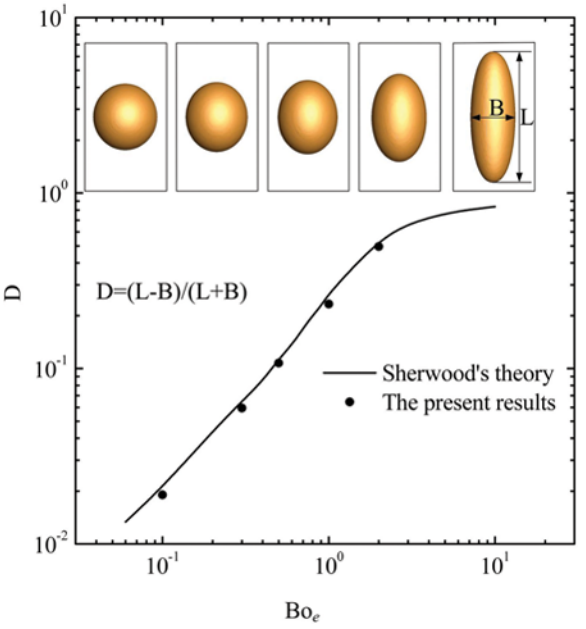

Figure 3. Comparison of the numerical results and the theoretical prediction of the deformations of a droplet when $\lambda_\varepsilon = 0.2$.

electric field are governed by electric force, surface tension force, inertial force, viscous force, buoyancy force, and so on. Therefore, we study the effects of the electric field, ratio of electrical permittivity, surface tension coefficient, and viscosity on the bubble motion and deformation. The computational model and boundary conditions are shown in Figure 1. The VOSET method is implemented on the grid resolution $R/\Delta = 15$, and the parameters λ_ρ and λ_μ are equal to 100 and keep constant.

3.1. Effect of Electric Force on Bubble Motion and Deformation

The effect of electric field on the motion and deformation of the bubble is investigated by changing the electric Bond number. Figure 4 shows the deformation history of the bubble at different $\mathrm{Bo_e}$ with the same flow conditions of $\mathrm{Re} = 2$, $\mathrm{Bo} = 2$, and $\lambda_\varepsilon = 3$. The bubble shapes in the absence of an electric field are presented in Figure 4*a*. At the initial stage, the deformation and accelerated rising of the bubble are because of the disequilibrium of surface tension force, inertial force, viscous force, and buoyancy force. After the force equilibrium is achieved, the bubble takes an ellipsoidal shape and rises steadily. When a uniform electric field is imposed in the vertical direction, the bubble (Figure 4*b*–4*c*) is stretched along the direction of the electric field by the electric force. The stronger electric field leads to larger deformation and rising velocity, which are shown in Figure 5. H and W are the bubble height and width, respectively. H/W reflects the deformation degree of the bubble, which increases with $\mathrm{Bo_e}$ because the bubble is stretched by the electric force overcoming the surface tension force. $A_\mathrm{W} = 0.125\pi W^2$ is the largest horizontal

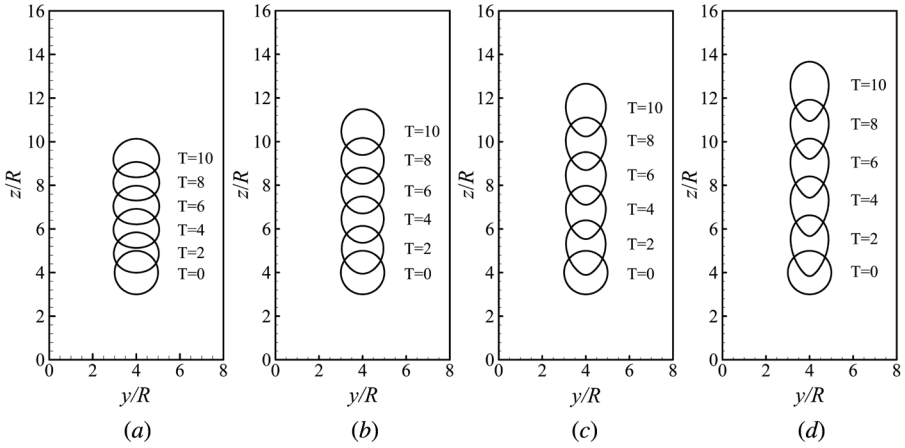

Figure 4. Evolution of the bubble shape for different electric Bond numbers. (*a*) $\mathrm{Bo_e} = 0$; (*b*) $\mathrm{Bo_e} = 5$; (*c*) $\mathrm{Bo_e} = 10$; (*d*) $\mathrm{Bo_e} = 15$.

cross-section of the bubble, which decreases with $\mathrm{Bo_e}$. The decrease of A_W leads to the decrease of the flow resistance and the increase of the bubble's rising velocity. The dimensionless velocities ($U = u/\sqrt{R\mathbf{g}}$) of the top and bottom of the bubble are shown in Figure 5*a*. When $T < 2$ and $\mathrm{Bo_e} = 0$, U_t and U_b increase rapidly, and U_t is larger than the U_b. When imposing the electric field in the vertical direction, a larger electric field leads to a faster increase of U_t. The increase of U_b delays with the increase of $\mathrm{Bo_e}$. After $T > 7$, the bubble has a steady rising velocity.

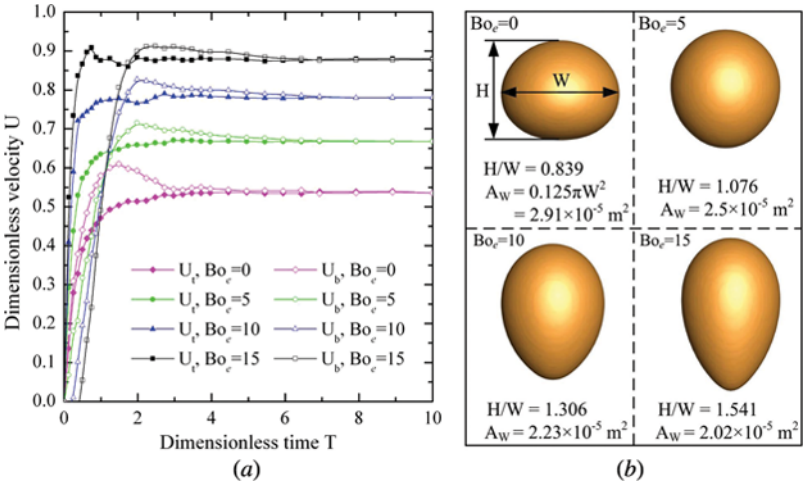

Figure 5. Rising velocity and deformation of the bubble for different electric Bond numbers: (*a*) the rising velocity U_t of the top of the bubble and the rising velocity U_b of the bottom of the bubble; (*b*) the size of the bubble.

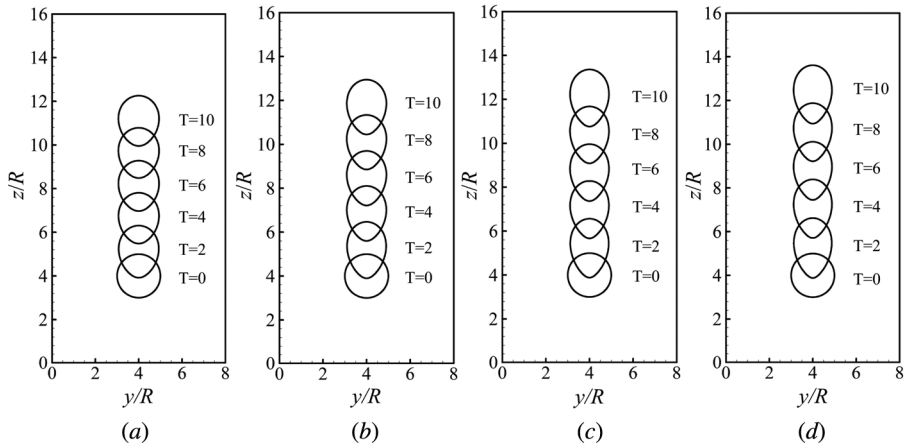

Figure 6. Evolution of the bubble shape for different ratios of electrical permittivity: (*a*) $\lambda_\varepsilon = 5$; (*b*) $\lambda_\varepsilon = 10$; (*c*) $\lambda_\varepsilon = 20$; (*d*) $\lambda_\varepsilon = 40$.

In literature [35], it can be found that the ratio of electrical permittivity has a significant influence on the electric force besides the electric field. Substituting the electric permittivity from Eq. (6) into Eq. (13), the electric force can be rewritten as

$$\mathbf{F}_e = -\frac{1}{2}\varepsilon_0\varepsilon_c \mathrm{E}^2 \nabla\left(\frac{1}{H(\phi) + \lambda_\varepsilon(1 - H(\phi))}\right) \tag{15}$$

The effect of the ratio of the electrical permittivity on bubble motion and deformation can be seen in Figure 6. In this investigation, the electric Bond number $\mathrm{Bo_e} = 5$, Reynolds number $\mathrm{Re} = 2$, and gravitational Bond number $\mathrm{Bo} = 2$ are constant. A larger λ_ε results in a larger bubble deformation, and this means that the electric force increases with λ_ε. Compared with Figure 6*a*–6*d*, it can be seen that the bottom of the bubble becomes sharper with increase of λ_ε. This is because the influence of the electric force is much larger than that of the surface tension force. The largest horizontal cross-section (A_W) of the bubble gradually decreases and results in the decrease of the flow resistance, so the rising velocity of the bubble increases.

3.2. Effect of Surface Tension Force on Bubble Motion and Deformation

The effect of surface tension force on the motion and deformation of the bubble is shown in Figure 7. In the present study, the change of the surface tension coefficient would change the values of the gravity Bond (Bo) number and the electric Bond ($\mathrm{Bo_e}$) number, but the Reynolds number $\mathrm{Re} = 2$, the ratio of the electrical permittivity $\lambda_\varepsilon = 3$, and the electric field intensity $\mathbf{E}_0 = 607{,}858\ \mathrm{V/m}$ still remain unchanged. Compared with Figure 7*a*–7*d*, it can be found that the decrease of the surface tension coefficient does not lead to a larger stretching deformation of the bubble, and the rising velocity of the bubble has no significant change. According

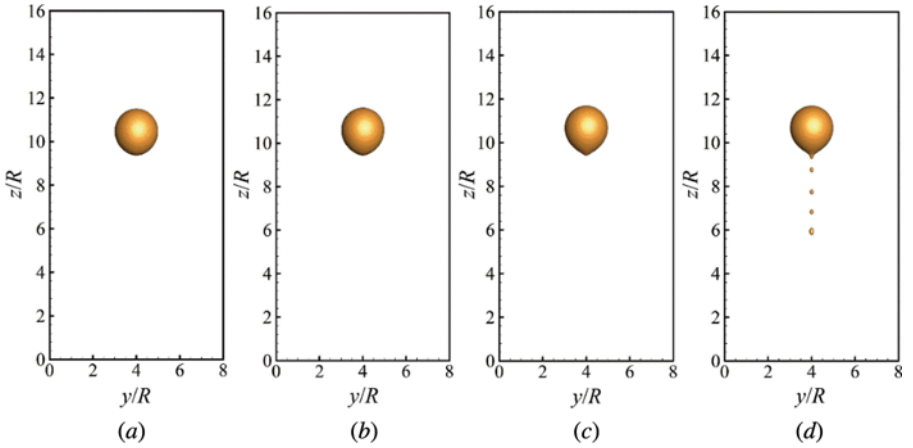

Figure 7. Effect of surface tension force on the bubble deformation ($T = 10$): (*a*) Bo = 2; (*b*) Bo = 4; (*c*) Bo = 8; (*d*) Bo = 16.

to the results in literature [39, 43], when the effect of the surface tension force is gradually weakened, the magnetic/electric force will overcome the surface tension force and stretch the droplet. However, a similar phenomenon has not been found in the present study because decrease of the effect of the surface tension force results in the increase of the effect of the buoyance force. Figure 8 shows the bubble shape

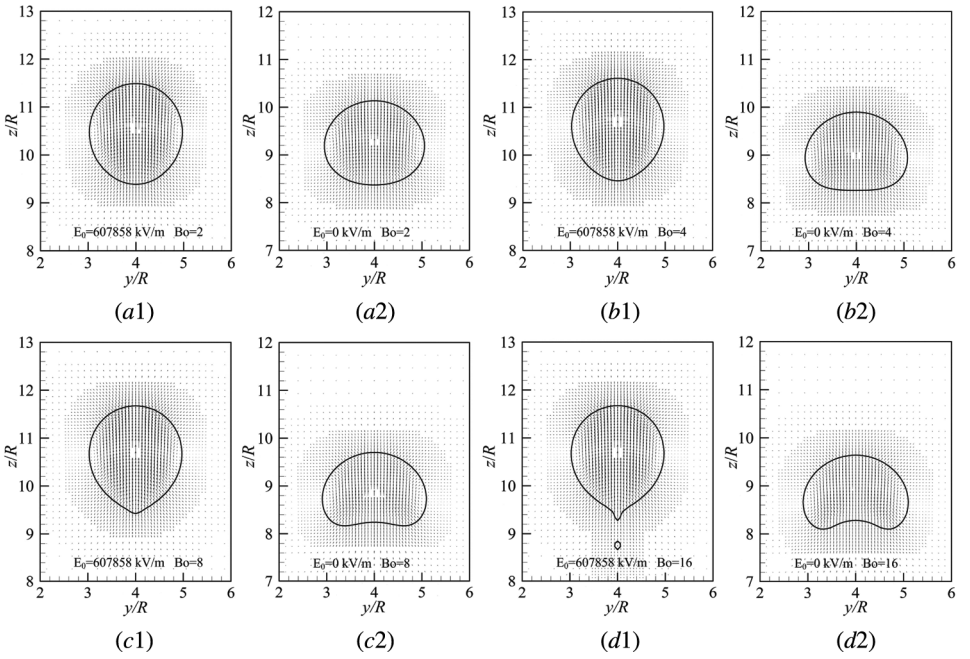

Figure 8. The velocity field and deformation of the bubble with different surface tension coefficients under the electric field $\mathbf{E}_0 = 607858\,\mathrm{kV/m}$ and $\mathbf{E}_0 = 0\,\mathrm{kV/m}$.

($T = 10$) when $E_0 = 607{,}858\ \mathrm{V/m}$ and $0\ \mathrm{V/m}$; it can be seen that in the absence of an electric field, the wake flow of the bubble has a stronger impulsive effect with the decrease of the surface tension coefficient. After imposing electric field, the electric force needs to overcome the stronger wake flow, so the bubble shapes in Figure 7 have no significant change; the bottom of the bubble only becomes more and more acute, and the satellite bubbles finally are produced.

3.3. Effect of Viscous Force on Bubble Motion and Deformation

Viscous force is an important factor to affect the motion and deformation of the bubble, and the deformation histories of the bubble at different Re with the same flow conditions of $\mathrm{Bo} = 2$, $\lambda_\varepsilon = 3$ are shown in Figure 9. Figure 9*a*1–9*d*1 shows the bubble rising in the absence of an electric field ($\mathrm{Bo_e} = 0$), and the bubble motions are governed by surface tension force, inertial force, viscous force, and buoyancy force. With the increase of the Reynolds number, the ultimate bubble shape gradually becomes an oblate ellipsoid, because the viscous drag gradually decreases and the buoyancy force has a more important effect. As shown in Figure 9*a*2–9*d*2, if a uniform electric field is imposed on the vertical direction, the bubble is stretched along the direction of the electric field. When increasing the electric field intensity (as shown in Figure 9*a*3–9*d*3), the bubble has a larger deformation and rising velocity. Compared with Figure 9*d*1–9*d*3, when the dimensionless time T equals 2, the bottom of the bubble gradually presents an arc with the increase of the electric Bond ($\mathrm{Bo_e}$) number. To further investigate and analyze this phenomenon, the deformation and rising of the bubble under larger electric fields are simulated.

Figure 10 shows the velocity field and deformation of the bubble at different times with the conditions of $\mathrm{Re} = 40$, $\mathrm{Bo} = 2$, $\mathrm{Bo_e} = 10$, and $\mathrm{Bo_e} = 20$, and the vectors are magnified 0.8 times in Figure 10*a* and 0.4 times in Figure 10*b*. It can be seen that the electric force has an important influence on the deformation at the initial stage of the bubble rising. When $\mathrm{Bo_e}$ equals 10 (as shown in Figure 10*a*), the bubble is stretched in the vertical direction, resulting in the formation of a teardrop shape at $T = 0.75$. Subsequently, the bottom of the bubble has an accelerated rising under the effects of the surface tension force and inertial force. The intensity of the jet above the bubble gradually increases to push the bottom of the bubble. When $T > 1.25$, the intensity of the jet gradually decreases, and the bubble gradually tends to a steady rising. If increasing the electric field such as $\mathrm{Bo_e} = 20$, the electric force, which is very large, can overcome the surface tension force and the jet above the bubble to produce a satellite bubble. The intensity of the jet in Figure 10*b* is larger than that in Figure 10*a*, and the surface tension force and electric force cannot resist the deformation of the bottom of the leading bubble. Finally, the leading bubble breaks up and has a toroidal shape.

Some attempts are made to prevent the break up of the bubble. According to the case in Figure 10*b*, one attempt is that the electric field $\mathbf{E}_0 = 1{,}488{,}943\ \mathrm{V/m}$ is added at $T = 2$, and the evolution of the bubble shape is shown in Figure 11*a*. After suddenly imposing a larger electric field, the surface tension force and the jet above cannot resist the electric force, and the bubble is stretched along the vertical direction. The satellite bubbles, which are smaller than that in Figure 10*b*, are produced, and the leading bubble breaks up. In another attempt, the electric field $\mathbf{E}_0 = 372{,}236$,

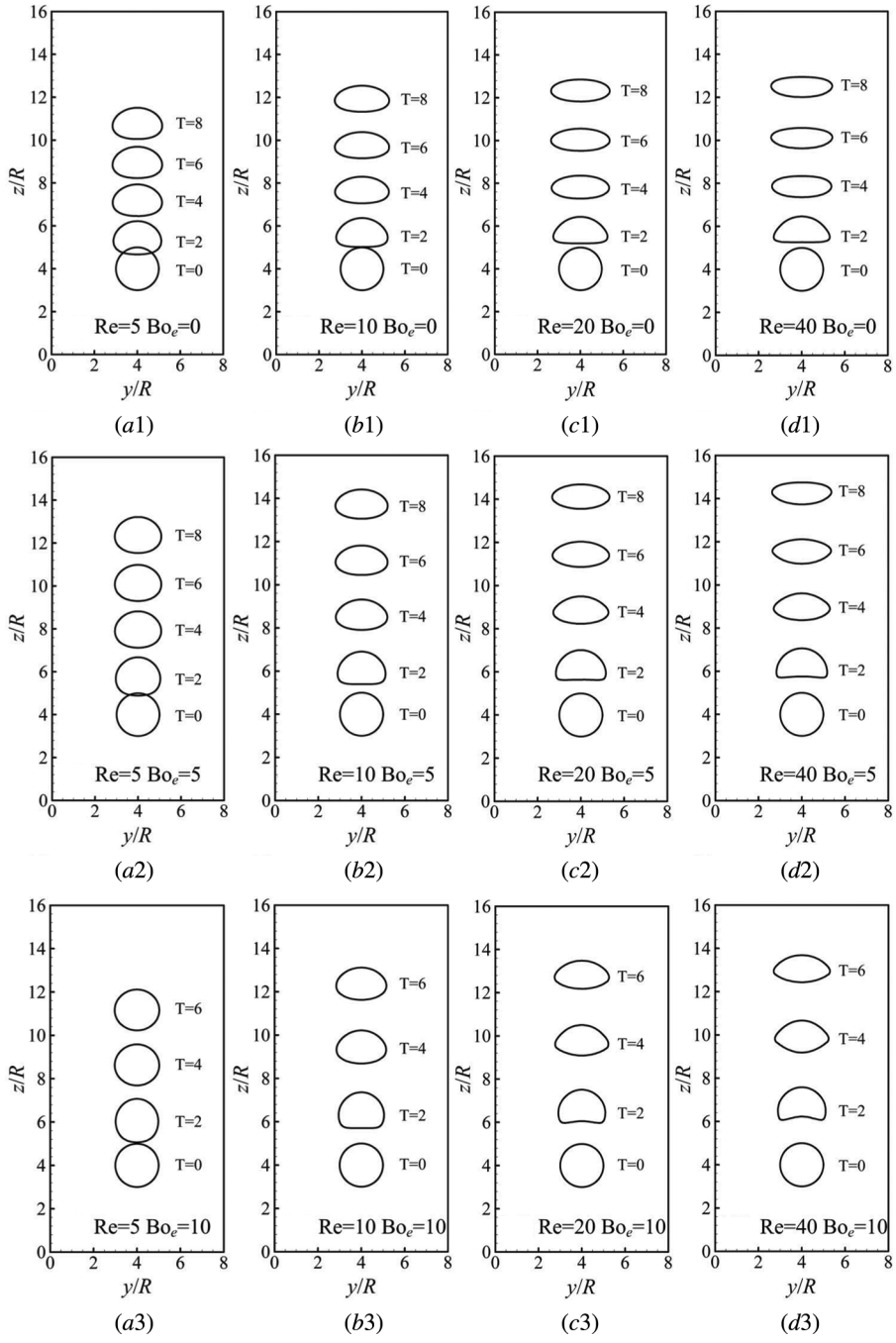

Figure 9. Evolution of the bubble shape for different Re and Bo_e.

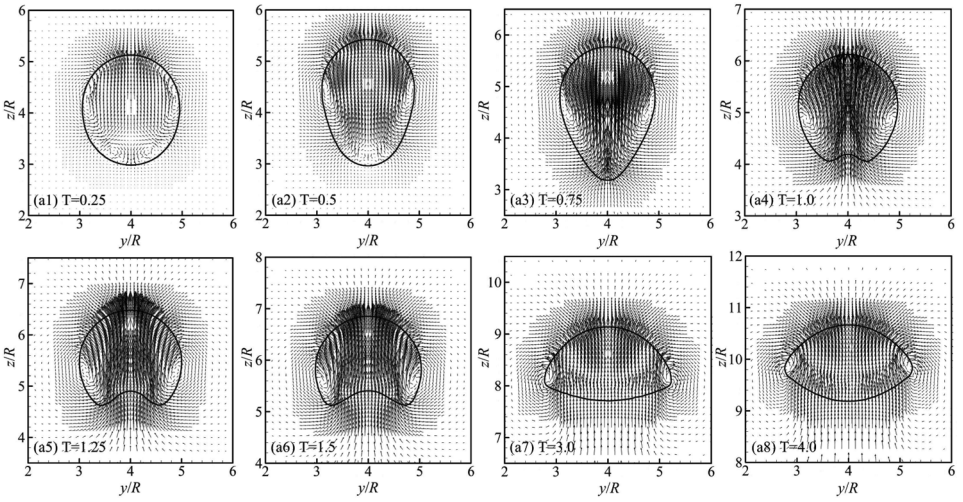

(*a*) Bo_e=10, Re=40, Bo=2

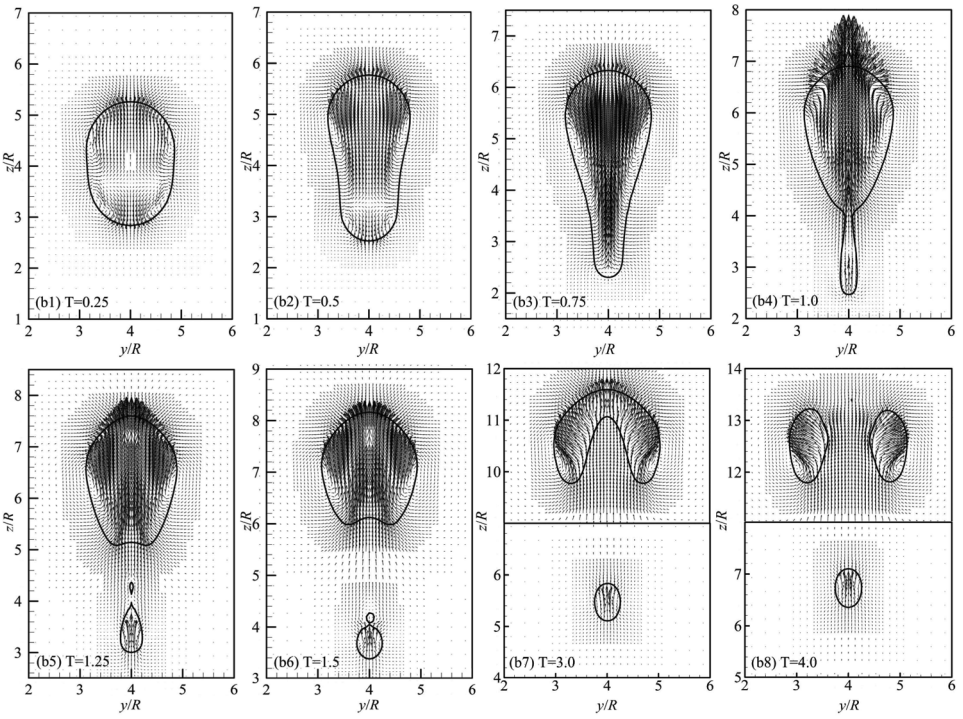

(*b*) Bo_e=20, Re=40, Bo=2

Figure 10. Velocity field and deformation of the bubble at different times.

744,471, 1,116,707, and 1,488,943 V/m are added at $T = 1$, 2, 3, 4, respectively. The results are shown in Figure 11*b*, it can be seen that the procedure of the deformation of the bubble is relatively smooth, and the break-up of the bubble is prevented.

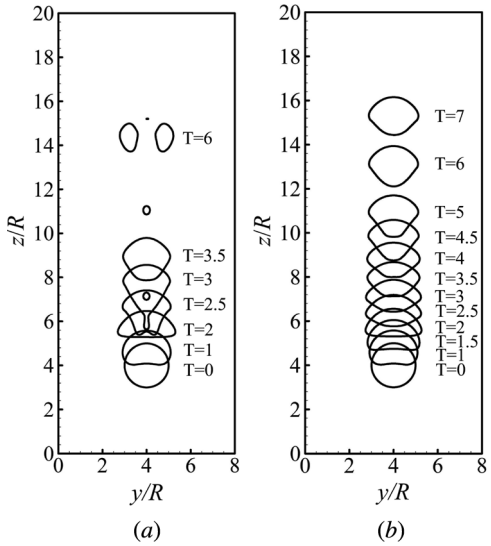

Figure 11. Evolution of the bubble shape for different attempts with $Bo_e = 20$, $Re = 40$, and $Bo = 2$: (*a*) the electric field $\mathbf{E}_0 = 1{,}488{,}943\,V/m$ is added at $T = 2$; (*b*) the electric fields $\mathbf{E}_0 = 372{,}236\,V/m$, $744{,}471\,V/m$, $1{,}116{,}707\,V/m$, and $1{,}488{,}943\,V/m$ are added at $T = 1$, 2, 3, and 4, respectively (The computational domain is $8R \times 8R \times 20R$).

4. CONCLUSIONS

In this article, a 3D coupled VOF and LS (3D-VOSET) method is used to investigate the effect of a uniform electric field on the dynamics behavior of bubbles in a viscous fluid. The VOSET method, which overcomes the disadvantages of the VOF and LS methods, conserves mass and accurately calculates the body forces and physical properties near the interfaces. The Poisson equation and the N–S equations are solved by the finite-volume method. The adaptive octree grid method is used to refine the region around the interface, and this adaptive local grid refinement technique can effectively improve the accuracy of the calculation and save the computer resources.

To test the 3D model, the equilibrium shape of a droplet in uniform electric fields is simulated, and the results show that the model in this article can accurately simulate the two-phase flow under electric fields. The effects of the electric field, ratio of electrical permittivity, surface tension coefficient, and viscosity on the bubble motion and deformation are investigated. It is found that the electric force stretches the bubble along the direction of the electric field. The stronger electric field or the higher ratio of electrical permittivity leads to larger bubble deformation and rising velocity. With the decrease of the surface tension coefficient, the bubble has no significant deformation. The viscous drag gradually decreases with the increase of the Reynolds number, and the electric force and buoyancy force have more important effects. For the case of a smaller Reynolds number, the electric force induces a larger deformation at the initial stage of the deformation of the bubble, and the bubble will break up when the electric force is larger. Two methods are adopted to prevent the

break up of the bubble. One method is that the electric field is added at $T = 2$, and this method cannot overcome the break-up of the bubble, so it is not a very effective method. In another method, the electric field is gradually added at a different time, and it can effectively prevent the break-up of the bubble, owing to the fact that the slow increase of the electric force induces the smaller deformation of the bubble.

FUNDING

This work was supported by the National Natural Science Foundation of China (No. 51176153), and the open fund of State Key Laboratory of Multiphase Flow in Power Engineering.

REFERENCES

1. R. Clift, J. R. Grace, and M. Weber, Bubbles, *Drops and Particles*, Academic Press, New York, 1978.
2. M. Wu and M. Gharib, Experimental Studies on the Shape and Path of Small Air Bubbles Rising in Clean Water, *Phys. Fluids*, vol. 14, pp. 49–52, 2002.
3. G. Brereton and D. Korotney, Coaxial, and Oblique Coalescence of Two Rising Bubbles, in I. Sahin, and G. Tryggvason (eds.), Dynamics of Bubbles, and Vortices Near a Free Surface, *AMD*, vol. 119, ASME, New York, 1991.
4. L. Amaya-Bower and T. Lee, Single Bubble Rising Dynamics for Moderate Reynolds Number Using Lattice Boltzmann Method, *Comp. Fluids*, vol. 39, pp. 1191–1207, 2010.
5. M. van Sint Annaland, N. G. Deen, and J. A. M. Kuipers, Numerical Simulation of Gas Bubbles Behaviour Using a Three-Dimensional Volume of Fluid Method, *Chemical Engineering Science*, vol. 60, pp. 2999–3011, 2005.
6. S. U. Sarnobat, S. Rajput, D. D. Bruns, D. W. DePaoli, C. S. Daw, and K. Nguyen, The Impact of External Electrostatic Fields on Gas–Liquid Bubbling Dynamics, *Chem. Eng. Sci.*, vol. 59, pp. 247–258, 2004.
7. W. Dong, R. Y. Li, H. L. Yu, and Y. Y. Yan, An Investigation of Behaviours of a Single Bubble in a Uniform Electric field, *Exp. Thermal Fluid Sci.*, vol. 30, pp. 579–586, 2006.
8. E. Iacona, C. Herman, S. Chang, and Z. Liu, Electric Field Effect on Bubble Detachment in Reduced Gravity Environment, *Exp. Thermal Fluid Sci.*, vol. 31, pp. 121–126, 2006.
9. A. Cattide, G. P. Celata, P. Di Marco, and W. Grassi, Experimental Study on Bubble Detachment Under Variable Heat Load and the Action of Electric Field, *Fluid Dyn. Res.*, vol. 40, pp. 485–496, 2008.
10. S. D. Bari and A. J. Robinson, Adiabatic Bubble Growth in Uniform DC Electric Fields, *Exp. Thermal Fluid Sci.*, vol. 44, pp. 114–123, 2013.
11. M. Gao, P. Cheng, and X. Quan, An Experimental Investigation on Effects of an Electric Field on Bubble Growth on a Small Heater in Pool Boiling, *Int. J. Heat Mass Transfer*, vol. 67, pp. 984–991, 2013.
12. F. J. Higuera, Injection of Bubbles in a Quiescent Inviscid Liquid Under a Uniform Electric Field, *J. Fluid Mech.*, vol. 568, pp. 203–222, 2006.
13. M. Jalaal, B. Khorshidi, E. Esmaeilzadeh, and F. Mohammadi, Behavior of a Single Bubble in a Nonuniform D.C. Electric Field, *Chem. Eng. Commun.*, vol. 198, pp. 19–32, 2010.
14. H. B. Zhang, Y. Y. Yan, and Y. Q. Zu, Numerical Modelling of EHD Effects on Heat Transfer and Bubble Shapes of Nucleate Boiling, *Appl. Math. Modell.*, vol. 34, pp. 626–638, 2010.

15. S. Sunder and G. Tomar, Numerical Simulations of Bubble Formation from Submerged Needles Under Non-uniform Direct Current Electric Field, *Phys. Fluids*, vol. 25, pp. 102–104, 2013.
16. S. Mählmann and D. T. Papageorgiou, Buoyancy-Driven Motion of a Two-Dimensional Bubble or Drop Through a Viscous Liquid in the Presence of a Vertical Electric Field, *Theor. Comput. Fluid Dyn.*, vol. 23, pp. 375–399, 2009.
17. Q. Yang, Y. Liu, B. Q. Li, and Y. Ding, Effect of Electric Field on a 3D Rising Bubble in Viscous Fluids, Proc. ASME 2013 Heat Transfer Summer Conf, Minneapolis, MN, USA, pp. 1–8, 2013.
18. J. C. Baygents, N. J. Rivette, and H. A. Stone, Electrohydrodynamic Deformation and Interaction of Drop Pairs, *J. Fluid Mech.*, vol. 368, pp. 359–375, 1998.
19. E. Lac and G. M. Homsy, Axisymmetric Deformation and Stability of a Viscous Drop in a Steady Electric Field, *J. Fluid Mech.*, vol. 590, pp. 239–264, 2007.
20. S. D. Deshmukh and R. M. Thaokar, Deformation, Breakup and Motion of a Perfect Dielectric Drop in a Quadrupole Electric Field, *Phys. Fluids*, vol. 24, pp. 032105, 2012.
21. G. Tryggvason, B. Bunner, A. Esmaeeli, D. Juric, N. Al-Rawahi, W. Tauber, J. Han, S. Nas, and Y. J. Jan, A Front-Tracking Method for the Computations of Multiphase Flow, *J. Comput. Phys.*, vol. 169, pp. 708–759, 2001.
22. A. Fernaández, G. Tryggvason, J. Che, and S. L. Ceccio, The Effects of Electrostatic Forces on the Distribution of Drops in a Channel Flow: Two-Dimensional Oblate Drops, *Phys. Fluids*, vol. 17, pp. 093302, 2005.
23. J. Hua, L. K. Lim, and C.-H. Wang, Numerical Simulation of Deformation/Motion of a Drop Suspended in Viscous Liquids Under Influence of Steady Electric Fields, *Phys. Fluids*, vol. 20, pp. 113302, 2008.
24. A. Fernaández, Response of an Emulsion of Leaky Dielectric Drops Immersed in a Simple Shear Flow: Drops More Conductive than the Suspending Fluid, *Phys. Fluids*, vol. 20, pp. 043303, 2008.
25. Y. Q. Zu and Y. Y. Yan, A Numerical Investigation of Electrohydrodynamic (EHD) Effects on Bubble Deformation Under Pseudo-Nucleate Boiling Conditions, *Int. J. Heat Fluid Flow*, vol. 30, pp. 761–767, 2009.
26. J. M. López-Herrera, S. Popinet, and M. A. Herrada, A Charge-Conservative Approach for Simulating Electrohydrodynamic Two-Phase Flows Using Volume-of-Fluid, *J. Comput. Phys.*, vol. 230, pp. 1939–1955, 2011.
27. E. Bjørklund, The Level-Set Method Applied to Droplet Dynamics in the Presence of an Electric Field, *Comp. Fluids*, vol. 38, pp. 358–369, 2009.
28. O. Ghazian, K. Adamiak, and G. S. P. Castle, Numerical Simulation of Electrically Deformed Droplets Less Conductive than Ambient Fluid, *Colloids Surfaces A Physicochem. Eng. Aspects*, vol. 423, pp. 27–34, 2013.
29. O. Ghazian, K. Adamiak, G. S. Peter Castle, and Y. Higashiyama, Oscillation, Pseudo-Rotation and Coalescence of Sessile Droplets in a Rotating Electric Field, *Colloids Surfaces A Physicochemical and Engineering Aspects*, vol. 441, pp. 346–353, 2014.
30. Y. Lin, P. Skjetne, and A. Carlson, A Phase Field Model for Multiphase Electro-Hydrodynamic Flow, *Int. J. Multiphase Flow*, vol. 45, pp. 1–11, 2012.
31. Q. Yang, B. Q. Li, and Y. Ding, 3D Phase Field Modeling of Electrohydrodynamic Multiphase Flows, *Int. J. Multiphase Flow*, vol. 57, pp. 1–9, 2013.
32. M. Sussman and E. G. Puckett, A Coupled Level Set and Volume-of-Fluid Method for Computing 3D and Axisymmetric Incompressible Two-Phase Flows, *J. Comput. Phys.*, vol. 162, pp. 301–337, 2000.
33. M. Sussman, A Second Order Coupled Level Set and Volume-of-Fluid Method for Computing Growth and Collapse of Vapor Bubbles, *J. Comput. Phys.*, vol. 187, pp. 110–136, 2003.

34. S. W. J. Welch and G. Biswas, Direct Simulation of Film Boiling Including Electrohydrodynamic Forces, *Phys. Fluids*, vol. 19, pp. 012106, 2007.
35. G. Tomar, D. Gerlach, G. Biswas, N. Alleborn, A. Sharma, F. Durst, S. W. J. Welch, and A. Delgado, Two-Phase Electrohydrodynamic Simulations Using a Volume-of-Fluid Approach, *J. Comput. Phys.*, vol. 227, pp. 1267–1285, 2007.
36. Z. Wang, J. Yang, B. Koo, and F. Stern, A Coupled Level Set and Volume-of-Fluid Method for Sharp Interface Simulation of Plunging Breaking Waves, *Int. J. Multiphase Flow*, vol. 35, pp. 227–246, 2009.
37. D. L. Sun and W. Q. Tao, A Coupled Volume-of-Fluid and Level Set (VOSET) Method for Computing Incompressible Two-Phase Flows, *Int. J. Heat Mass Transfer*, vol. 53, pp. 645–655, 2010.
38. T. Wang, H. X. Li, Y. C. Feng, and D. X. Shi, A Coupled Volume-of-Fluid and Level Set (VOSET) Method on Dynamically Adaptive Quadtree Grids, *Int. J. Heat Mass Transfer*, vol. 67, pp. 70–73, 2013.
39. D. Shi, Q. Bi, and R. Zhou, Numerical Simulation of a Falling Ferrofluid Droplet in a Uniform Magnetic Field by the VOSET Method, *Numer. Heat Transfer Part A: Appl.*, vol. 66, pp. 144–164, 2014.
40. R. Singh and W. Shyy, Three-Dimensional Adaptive Cartesian Grid Method with Conservative Interface Restructuring and Reconstruction, *J. Comput. Phys.*, vol. 224, pp. 150–167, 2007.
41. N. Nikolopoulos, A. Theodorakakos, and G. Bergeles, Three-Dimensional Numerical Investigation of a Droplet Impinging Normally onto a Wall Film, *J. Comput. Phys.*, vol. 225, pp. 322–341, 2007.
42. D. Fuster, A. Bagué, T. Boeck, L. Le Moyne, A. Leboissetier, S. Popinet, P. Ray, R. Scardovelli, and S. Zaleski, Simulation of Primary Atomization with an Octree Adaptive Mesh Refinement and VOF Method, *Int. J. Multiphase Flow*, vol. 35, pp. 550–565, 2009.
43. J. D. Sherwood, Breakup of Fluid Droplets in Electric and Magnetic-Fields, *J. Fluid Mech.*, vol. 188, pp. 133–146, 1988.
44. T. Wang, H. Li, and Y. Li, Numerical Investigation on Coaxial Coalescence of Two Gas Bubbles, *J. Xi'an Jiaotong Univ.*, vol. 47, pp. 1–6, 2013.
45. J. U. Brackbill, D. B. Kothe, and C. Zemach, A Continuum Method for Modeling Surface-Tension, *J. Comput. Phys.*, vol. 100, pp. 335–354, 1992.